Role of Hidden Spin Polarization in Nonreciprocal Transport of Antiferromagnets

Weizhao Chen,[1] Mingqiang Gu[⦿],[1] Jiayu Li,[1] Panshuo Wang,[1] and Qihang Liu[⦿][1,2,3,*]

[1]*Shenzhen Institute for Quantum Science and Engineering and Department of Physics,*
Southern University of Science and Technology, Shenzhen 518055, China
[2]*Guangdong Provincial Key Laboratory of Computational Science and Material Design,*
Southern University of Science and Technology, Shenzhen 518055, China
[3]*Shenzhen Key Laboratory of Advanced Quantum Functional Materials and Devices,*
Southern University of Science and Technology, Shenzhen 518055, China

The discovery of hidden spin polarization (HSP) in centrosymmetric nonmagnetic crystals, i.e., spatially distributed spin polarization originated from local symmetry breaking, has promised an expanded material pool for future spintronics. However, the measurements of such exotic effects have been limited to subtle space- and momentum-resolved techniques, unfortunately, hindering their applications. Here, we theoretically predict macroscopic non-reciprocal transports induced by HSP when coupling another spatially distributed quantity, such as staggered local moments in a space-time PT-symmetric antiferromagnet. By using a four-band model Hamiltonian, we demonstrate that HSP plays a crucial role in determining the asymmetric bands with respect to opposite momenta. Such band asymmetry leads to non-reciprocal nonlinear conductivity, exemplified by tetragonal CuMnAs via first-principles calculations. We further provide the material design principles for large nonlinear conductivity, including two-dimensional nature, multiple band crossings near the Fermi level, and symmetry protected HSP. Our Letter not only reveals direct spintronic applications of HSP (such as Néel order detection), but also sheds light on finding observables of other hidden effects, such as hidden optical polarization and hidden Berry curvature.

Introduction.—According to the seminal works of Dresselhaus and Rashba, spin polarization in nonmagnetic crystals that lack inversion symmetry P is possible due to the relativistic spin-orbit coupling (SOC) [1,2]. Recent studies revealed that a related form of hidden spin polarization (HSP) should exist even in centrosymmetric crystals, as long as atomic sites individually break inversion symmetry locally [3,4]. Such an HSP effect could significantly expand the pool of potential materials for spintronics [5,6], and provide new physical insights into the relevant hidden physics such as optical polarization, valley polarization, orbital polarization, Berry curvature, etc. [7–17]. Owing to the coexistence of P and time-reversal symmetry T, the HSP in nonmagnetic materials localized at a sector $\boldsymbol{P}_k(r)$ is odd distributed in both real and momentum spaces, i.e., $\boldsymbol{P}_k(r) = -\boldsymbol{P}_k(-r)$ and $\boldsymbol{P}_k(r) = -\boldsymbol{P}_{-k}(r)$. Therefore, while HSP has been successfully measured by techniques with both $\boldsymbol{r}$- and $\boldsymbol{k}$-resolution, such as spin- and angle-resolved photoemission spectroscopy [18–26], its application in spintronics requires global symmetry breaking (e.g., via external electric fields) to release the compensation of polarization originated from the high global symmetry [3,27].

To utilize the HSP effect for a macroscopic observation requires breaking both sector and momentum compensation conditions described above, rendering a challenging

issue if the global symmetry is maintained. Here, we propose a way to manipulate HSP $\boldsymbol{P}_k(r)$ by coupling another odd-distributed quantity $\boldsymbol{M}(r)$. The resultant observable $O(r) = \int \boldsymbol{P}_k(r) \cdot \boldsymbol{M}(r)$ yields a superposition effect between the two sectors rather than compensation. Specifically, when $\boldsymbol{M}(r)$ represents the staggered Néel order in antiferromagnetic (AFM) materials, the absence of T also removes the momentum compensation, leading to possible spin-orbitronic applications. Recently, the coupling between the AFM order and SOC-induced spin texture is predicted to induce a spin-orbit torque that can, in turn, switch the Néel order electrically in antiferromagnets CuMnAs and Mn_2Au [28,29]. However, a following experimental study suggested that the thermal effect may reduce the reliability of such electrical switching [30].

In this Letter, we investigate the non-reciprocal transport in PT-symmetric antiferromagnets, in which every band is spin degenerate, yet exhibiting HSP effects due to the local symmetry breaking. Starting from a four-band model and Boltzmann transport theory, we elucidate that, by coupling the staggered AFM magnetization, HSP is not only the trigger of non-reciprocal transport, but also determines the magnitude of the non-reciprocal nonlinear current (NLC) via the pivot of band asymmetry between opposite

momenta $\pm k$. To demonstrate our theory, we apply first-principles calculations to simulate the NLC of tetragonal CuMnAs, yielding qualitatively consistent results with the recent experiment [31], and quantitatively identifying the crucial role of HSP. Then, we provide the design principle of antiferromagnets with large NLC, including large HSP that could be protected by nonsymmorphic symmetry, band crossings or anticrossings around the Fermi surface, and the nature of low dimension. Our finding reveals a macroscopic observable of HSP whose identification is previously limited to space and momentum resolved measurements, paving an avenue for HSP materials in the applications of future AFM spintronics.

Coupling between hidden SOC and Néel order.—To elucidate the coupling between the HSP effect and Néel order, we consider PT-symmetric antiferromagnets. While the global PT symmetry ensures spin degeneracy throughout the whole Brillouin zone (BZ), in real space, there could be "sectors" breaking PT locally and, thus, manifesting spin polarization owing to the relativistic SOC anchored on the nuclear sites. Such a concept of HSP is originally proposed and classified via crystallographic group in nonmagnetic materials with inversion symmetry [4], but can be easily extended to PT-symmetric antiferromagnets. Taking the tetragonal structure of CuMnAs as an example [Fig. 1(a)], the two Mn atoms (site symmetry 4 mm) in a unit cell with opposite in-plane magnetizations are symmetric with respect to the PT center, thus, belonging to two sectors α and β, respectively. Therefore, the HSP is defined by projecting the Bloch wave functions ψ_{nk} of the doubly degenerate bands onto a specific sector, say α, $P_k^\alpha = \sum_{i\in\alpha} \sum_{n\in\mathbb{N}} \langle \psi_{nk} | \boldsymbol{\sigma} \otimes |i\rangle\langle i| \psi_{nk}\rangle$, where k, $\boldsymbol{\sigma}$, and $|i\rangle$ denote the wave vector, Pauli operator for spin degree of freedom, and the localized orbitals belonging to sector α, respectively. $\mathbb{N}$ denotes the summation over the two
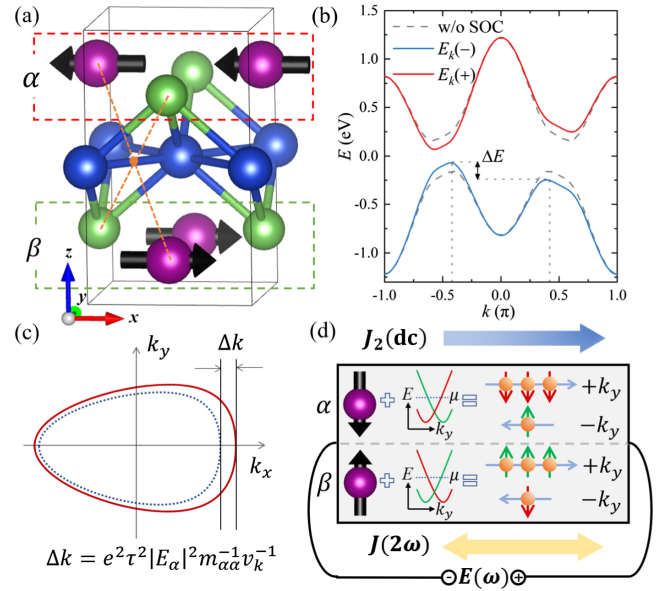

FIG. 1. (a) Crystal structure of CuMnAs as an example of PT-symmetric antiferromagnets with two sectors α and β connected by PT center with orange dashed lines. (b) The band structure of the four-band Hamiltonian with band asymmetry. The parameters used for calculation are $t_k = \cos^2 k$, $\epsilon_k = 0.2\cos k$, $M = 0.2$, and $\lambda_k = 0.1 \sin k$ for SOC. (c) Schematic plot of the Fermi surface expansion or shrinking due to the second-order effect of the electric field E_α. (d) Schematic plot of the formation of longitudinal nonlinear current, which is originated from the coupling between HSP and staggered magnetization. The red bands possess spin down polarization as the red arrows adhere to the carriers on the right hand, and spin up polarization is denoted by the green arrows.

degenerate bands, implying that P_k^α is independent of the choice of the wave function basis.

Then, we construct a four-band model Hamiltonian containing both HSP and Néel order as follows:

$$
H = \begin{pmatrix}
\epsilon_k^\alpha & [(\boldsymbol{\lambda_k} + \boldsymbol{M})\cdot\boldsymbol{\sigma}]_{12} & t_k & 0 \\
[(\boldsymbol{\lambda_k} + \boldsymbol{M})\cdot\boldsymbol{\sigma}]_{12}^* & \epsilon_k^\alpha & 0 & t_k \\
t_k^* & 0 & \epsilon_k^\beta & -[(\boldsymbol{\lambda_k} + \boldsymbol{M})\cdot\boldsymbol{\sigma}]_{12} \\
0 & t_k^* & -[(\boldsymbol{\lambda_k} + \boldsymbol{M})\cdot\boldsymbol{\sigma}]_{12}^* & \epsilon_k^\beta
\end{pmatrix},
\tag{1}
$$

where $\epsilon_k^\alpha = \epsilon_k^\beta = \epsilon_k$ is the on-site energy and t_k is the wave function hybridization between the two sectors. $\boldsymbol{\lambda_k}$ and $\boldsymbol{M}$ denote the effective magnetic field caused by SOC and the local moment, respectively. For example, classic Rashba and Dresselhaus effects correspond to $\boldsymbol{\lambda_k} = \alpha_R(k_y, -k_x, 0)$ and $\boldsymbol{\lambda_k} = \alpha_D(k_x, -k_y, 0)$, respectively. The subscript "12" represents the off-diagonal element of the two-rank matrix, i.e., $[(\boldsymbol{\lambda_k} + \boldsymbol{M})\cdot\boldsymbol{\sigma}]_{12} = (\lambda_{k,x} + M_x) - i(\lambda_{k,y} + M_y)$. Since PT symmetry is conserved, there are

the two sets of doubly degenerate bands with the eigenvalues $E_k(\pm) = \epsilon_k \pm \sqrt{|\boldsymbol{\lambda_k} + \boldsymbol{M}|^2 + |t_k|^2}$, as shown in Fig. 1(b). The corresponding HSPs are $P_k(\pm) = \pm(\boldsymbol{\lambda_k} + \boldsymbol{M})/\sqrt{|\boldsymbol{\lambda_k} + \boldsymbol{M}|^2 + |t_k|^2}$, indicating that the hybridization between sectors t_k is detrimental to the magnitude of HSP.

A key condition to have a nonzero macroscopic observable such as non-reciprocal carrier transport is the band asymmetry with respect to opposite vectors,

i.e., $E_k \neq E_{-k}$ [32,33]. While such a condition is fulfilled when both P and T are broken, its magnitude, namely, $\Delta E = E_k - E_{-k}$, is not determined by symmetry arguments and remains unclear. According to Eq. (1), we analytically obtain

$$\Delta E(\pm) = \frac{\pm 4 P_k^{\text{ave}} \boldsymbol{\lambda_k} \cdot \boldsymbol{M}}{|\boldsymbol{\lambda_k} + \boldsymbol{M}| + |\boldsymbol{\lambda_k} - \boldsymbol{M}|}, \tag{2}$$

where $P_k^{\text{ave}} = \{w|P_{+k}^\alpha| + (1-w)|P_{-k}^\alpha|\}$ is the weighted average of HSP with the weight $w = \sqrt{|\boldsymbol{\lambda_k} + \boldsymbol{M}|^2 + |t_k|^2}/ \{\sqrt{|\boldsymbol{\lambda_k} + \boldsymbol{M}|^2 + |t_k|^2} + \sqrt{|\boldsymbol{\lambda_k} - \boldsymbol{M}|^2 + |t_k|^2}\}$. From Eq. (2), we find that when $\boldsymbol{\lambda_k}$ is parallel to $\boldsymbol{M}$, the band asymmetry $\Delta E = 2 \min\{|\boldsymbol{\lambda_k}|, |\boldsymbol{M}|\} P_k^{\text{ave}}$ is proportional to the HSP. On the other hand, ΔE vanishes when $\boldsymbol{\lambda_k}$ is perpendicular to $\boldsymbol{M}$. Equation (2) clearly shows that in PT-symmetric antiferromagnets, the cooperation of magnetic order, SOC and local symmetry breaking as the key reason gives rise to band asymmetry, which further leads to a global non-reciprocal transport behavior, as discussed in the following.

Non-reciprocal nonlinear conductivity.—Unlike the first-order current caused by the drifting move, the second-order effect of the electric field $\boldsymbol{E}$ originates from the expansion or shrinking of the Fermi surface due to carrier acceleration. In this way, an asymmetric Fermi surface caused by band asymmetry leads to a net nonlinear current [Fig. 1(c)]. Expanding the Boltzmann equation to the second order with respect to $\boldsymbol{E}$ (see Supplemental Material Section A for details [34]), we obtain a nonlinear current $j_{2,\gamma} = \sum_{\alpha\beta} \sigma_{\gamma\alpha\beta} E_\alpha E_\beta$ with the second-order conductivity tensors for an energy band as follows:

$$\sigma_{\gamma\alpha\beta} = \frac{e^3 \tau^2}{V N_k} \sum_{k \in \text{BZ}} m_{\gamma\alpha}^{-1} v_\beta \frac{\partial f_0}{\partial \epsilon}, \tag{3}$$

where τ is the relaxation time and $m_{\gamma\alpha}^{-1} = (1/\hbar)(\partial v_\gamma / \partial k_\alpha)$ is the inverse effective mass with the group velocity v. We note that Eq. (3) describes the extrinsic NLC, which is equivalent to the other forms of the Drude term used in recent studies [42–45]. Nevertheless, Eq. (3) explicitly highlights the effective mass as another key ingredient of the nonlinear current.

As shown in Fig. 1(d), given a nonzero $\sigma_{\gamma\alpha\beta}$, an electric field $\boldsymbol{E}(\omega)$ would drive a nonlinear current $j_{2,\gamma}$ composed of an alternating current $J(2\omega)$ with the frequency of 2ω and a direct current J_2, leading to the unidirectional magneto-resistance effect [46–48]. Specifically, for CuMnAs, the forward and backward currents in the y direction carry opposite spin polarization ($\pm x$) due to the Rashba-type spin texture and, then, are scattered by the atomic magnetic moments (along x), resulting in a unidirectional current in a single sector. For the other sector, the cooperation of both reversed HSP and magnetic moment leads to a coherent effect. As a result, a longitudinal nonlinear current emerges along the y direction. With the symmetry analysis of Eq. (3)

(see Supplemental Material Section B [34]), nonzero σ_{yxx} and σ_{yzz} for the tetragonal CuMnAs are also allowed, indicating that both E_x and E_z can drive Hall-type nonlinear currents along y. The nonlinear current has been proposed to be a rectifier [32,33,49], while, in antiferromagnets, it can also be used as the reading head of the Néel order [31,42,50]. For a 180° rotation of Néel order, the local moments $\boldsymbol{M}$ are reversed while the local SOC fields $\boldsymbol{\lambda_k}$ are conserved. As a result, the coupling-induced NLC changes its sign. We note that such HSP-assisted NLC exists in antiferromagnets with PT symmetry, which forbids the nonlinear anomalous Hall effect originated from the Berry curvature dipole [50].

To further investigate the relationship between band asymmetry and nonlinear current, we simplify Eq. (3) and consider σ_{yyy} by assuming uniform dispersions along k_x and k_z

$$\sigma_{yyy} = \frac{e^3 \tau^2}{2\pi V} \{m_{yy}^{-1}(k_F^-) - m_{yy}^{-1}(k_F^+)\}$$
$$\approx \frac{e^3 \tau^2}{2\pi V} \left\{ \frac{\partial m_{yy}^{-1}}{\partial \epsilon}(k_F^-) \Delta E + \frac{\partial^2 \Delta E}{\partial k^2} \right\}, \tag{4}$$

where $k_F^+(k_F^-)$ is the Fermi vector with the positive (negative) group velocity. Equation (4) directly explains the relationship between NLC and the band asymmetry $\Delta E = E(k_F^-) - E(-k_F^-)$, which is characterized by HSP as discussed above. In addition, the first term indicates that large changes in effective mass, such as the tipping point caused by band crossing or anticrossing, could also enhance the conductivity. Next, we perform NLC calculations based on atomistic Hamiltonians obtained from density-functional theory to further illustrate the role of HSP in non-reciprocal transports (see Supplemental Material Section B [34]).

Nonlinear conductivity in CuMnAs.—We choose CuMnAs to identify the characteristics of non-reciprocal NLC and the role of HSP because it is a room-temperature, PT-symmetric, antiferromagnetic metal with intriguing Dirac fermions in various structures [51–53], rendering a nice platform for novel transport properties. While recent works have predicted its intrinsic nonlinear Hall effect, which is originated from the Berry connection [54,55], we focus on the extrinsic current related to impurities scattering that can be either longitudinal or transverse. In the following, we focus on the discussion of longitudinal NLC, i.e., σ_{yyy}, and leave the transverse NLC component σ_{yxx} to Supplemental Material Section C [34].

First, we calculate the NLC in a CuMnAs thin film with the thickness of two primitive cells and discuss the results of the bulk later. The calculated σ_{yyy} as a function of the chemical potential μ is shown in Fig. 2(a), where a large and sharp peak appears at $\mu = 0.22$ eV accompanied by some oscillations. To reveal the origin of this peak, we decompose σ_{yyy} onto the contributions from different bands
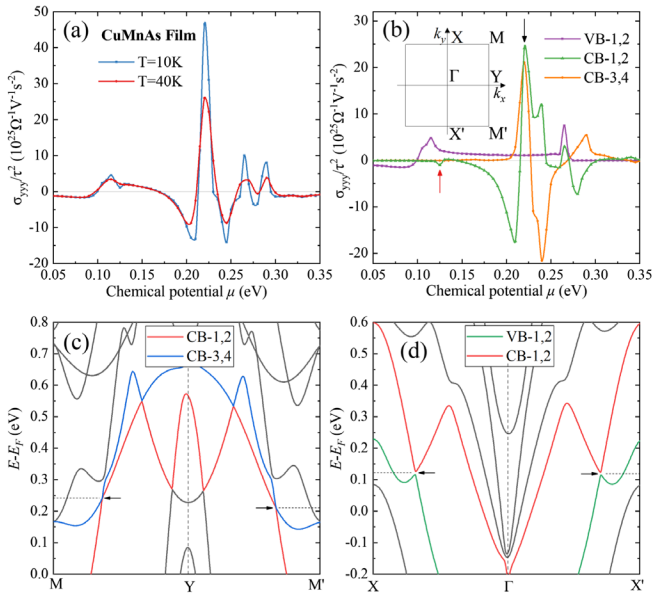
FIG. 2. (a) Nonlinear conductivity σ_{yyy} of CuMnAs film with a thickness of two primitive cells as a function of the chemical potential μ with different temperatures. (b) The band-decomposed σ_{yyy} of CuMnAs film, where a small peak and a large peak for CB-1,2 are marked by the red and black arrows, respectively. The inset shows the two-dimensional Brillouin zone. (c) Band structure for the k path along M-M', where the type-II Dirac points are marked by the black arrows. (d) Band structure for the k path along X-X', where the band anticrossings are marked by the black arrows.
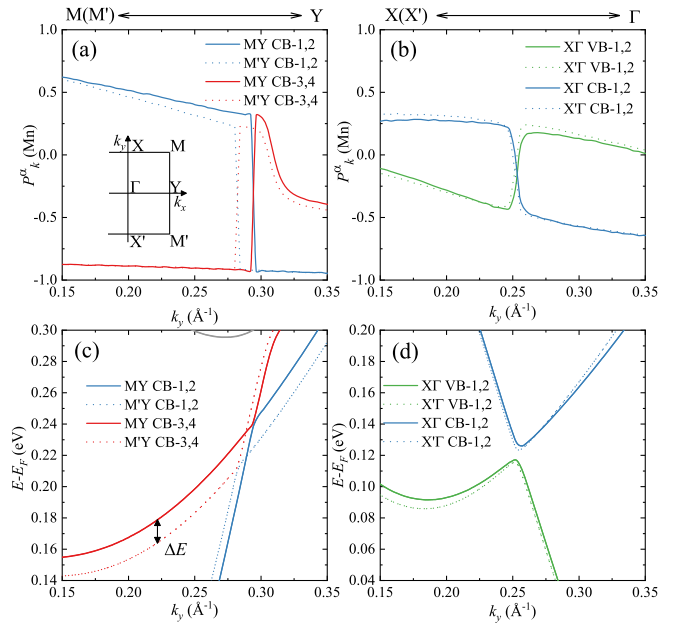
FIG. 3. (a) and (b) The magnitude of HSP $P_k^\alpha(\mathrm{Mn})$ for the corresponding bands in the k path along (a) M-M' with the type-II Dirac points and (b) X-X' with the band anticrossings. (c) and (d) The band structures of CuMnAs film for the k path along (c) M-M' with the type-II Dirac points and (d) X-X' with the band anticrossings. The bands are folded with respect to Y and Γ to show the band asymmetry ΔE clearly. The solid and dashed lines represent the k path M-Y (X-Γ) and M'-Y (X'-Γ), respectively.

around the Fermi energy. Three pairs of doubly degenerate bands, i.e., the highest valence bands VB-1,2, and thus, the lowest conduction bands CB-1,2 and CB-3,4 are involved. As shown in Fig. 2(b), around $\mu = 0.22$ eV the NLC from CB-1,2 shows a negative peak followed by a positive one, while that of CB-3,4 shows positive and negative peaks sequentially. The two positive peaks happen to overlap each other and contribute to the peak of total NLC as denoted by the black arrow in Fig. 2(b).

From the band structure shown in Fig. 2(c), we find that the band asymmetry between the M-Y and M'-Y ensures the existence of the NLC. Specifically, the Dirac cone along M-Y is 0.029 eV higher than that along M'-Y, as denoted by the black arrows in Fig. 2(c). These type-II Dirac points, formed by CB-1,2 and CB-3,4 around $\mu = 0.22$ eV, lead to the large NLC peaks in Fig. 2(b). Furthermore, the discontinuous effective masses induced by the Dirac points significantly enhance the NLC effect according to Eq. (4). We also notice that there is another small peak at $\mu \sim 0.12$ eV for the decomposed NLC from CB-1,2, as denoted by the red arrow in Fig. 2(b). This peak is caused by the band anticrossing between VB-1,2 and CB-1,2 along the k path X-X' as shown in Fig. 2(d).

Next, we project the Bloch wave functions onto the magnetic Mn atoms and calculate the HSP $P_k^\alpha(\mathrm{Mn})$. Figure 3(a) shows $P_k^\alpha(\mathrm{Mn})$ of CB-1,2 and CB-3,4 along

M-Y-M', where two Dirac points are clearly presented with a momentum offset, indicating the band asymmetry. We find that both bands manifest large HSP, with one of them approaching almost 100% polarization. In sharp contrast, $P_k^\alpha(\mathrm{Mn})$ of VB-1,2 and CB-1,2 along X-Γ-X' is much smaller, as shown in Fig. 3(b). Such a significant difference in HSP is caused by the nonsymmorphic structure of CuMnAs. The glide mirror reflection minimizes the spin compensation between different sectors at the boundary of the Brillouin zone M-Y-M', thus, retaining the HSP in each sector [6,26].

As shown in Eq. (2), the HSP closely correlates the band asymmetry ΔE. This is further illustrated in Figs. 3(c) and 3(d), where we fold the band structures along M-Y-M' and X-Γ-X' with respect to Y and Γ, respectively, with the bands with $\pm k_y$ plotted on top of each other. As shown in Fig. 3(c), the large band asymmetry ΔE (about 17 meV) is attributed to the nearly 100% $P_k^\alpha(\mathrm{Mn})$ around the Dirac cone, while ΔE around the band anticrossing in Fig. 3(d) is rather small with only 4 meV. As a result, the comparison between ΔE gives rise to the sharp contrast of the two peaks of NLC in Fig. 2(b), fully consistent with Eq. (4). The above analysis clearly highlights the significant role of HSP in the generation of nonlinear current: The required local symmetry breaking determines the existence of the nonlinear current in the AFM system with PT symmetry;
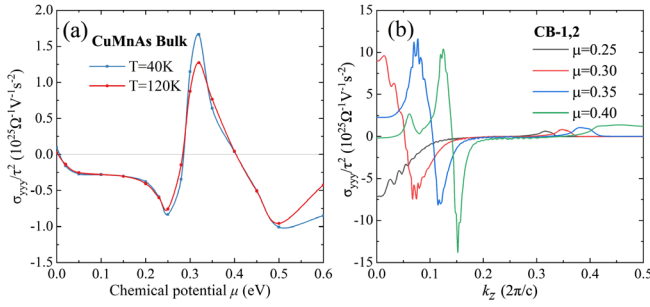
FIG. 4. (a) Nonlinear conductivity σ_{yyy} of Bulk CuMnAs as a function of chemical potential μ with different temperatures. (b) The k_z-resolved conductivity σ_{yyy} with different chemical potential μ.

more importantly, it is also a key factor to the magnitude of NLC. Since the NLC is an effect regarding the Fermi surface, the critical temperature depends on the competition between ΔE and the average thermal energy of carriers. Therefore, HSP also has an effect that resists the decreasing of NLC upon increasing temperature (see Supplemental Material Section D [34]).

Design principles.—Before uncovering the design principles of large non-reciprocal NLC, we calculate the NLC of 3D bulk CuMnAs for comparison. Figure 4(a) shows σ_{yyy} as a function of μ. It is found that, similar to the 2D case, at around $\mu = 0.3$ eV the type-II Dirac points induce a peak, which is 1 order of magnitude smaller than that of the thin film. To understand this, we resort to the k_z-resolved NLC. As shown in Fig. 4(b), the resolved σ_{yyy}, as the function of k_z, is composed of a positive peak followed by a negative peak, resulting in significant compensation over the integration. This feature essentially originates from the shift of Dirac cones in the energy scale with increasing k_z (see Supplemental Material Section E [34]), implying that a small energy dispersion along k_z or reducing the size from the bulk to thin film would suppress the compensation and, thus, enhance the magnitude of NLC.

Except for reducing the dimension, more design principles for PT-symmetric antiferromagnets with advanced non-reciprocal transport properties are also revealed by the case of CuMnAs. First, the NLC driven by HSP exists in all PT-symmetric antiferromagnets with breaking P in magnetic space groups (for 3D systems) and breaking both P and C_{2z} in magnetic layer groups (for quasi-2D systems). Second, nonsymmorphic symmetry could retain large HSP, which also determines the magnitude of band asymmetry and NLC. Moreover, the band crossing and anticrossing around the Fermi level serve as another amplifier of extrinsic NLC because of the large effective mass change. The above mentioned design principles would facilitate the search of material candidates with large NLC. Another candidate $Mn_2Bi_2Te_5$ is discussed in Supplemental Material Section F [34].

Discussion.—By coupling HSP with the Néel order of PT-symmetric antiferromagnets, we show that a macroscopic measurable quantity, such as non-reciprocal transport, could emerge. Such a finding expands the conventional detection of HSP that requires both space and momentum resolution, and proposes specific applications in antiferromagnetic spintronics, such as the identification and manipulation of Néel order [31]. Experimentally, the Néel order of HSP antiferromagnets could be detected through either dc or ac measurement. The nonlinear longitudinal dc could be measured by the unidirectional magnetoresistance based on a double Hall cross with a four-probe configuration [46], yet without applying an external magnetic field; while the nonlinear ac for both longitudinal and transversal components could be measured based on a Hall cross structure with lock-in amplifiers [31].

More importantly, the basic idea of cooperating two spatially odd-distributed quantities opens a new avenue for exotic phenomena in the systems with various hidden polarizations. For example, coupling between the electron velocity (odd in position space) and the local spin polarization leads to the second-order spin photogalvanic effect and inverse Faraday effect [56–58], which can be understood as an optical response in the HSP system. A more generic picture can be grasped by considering the orbital Hall effect in centrosymmetric materials, which originates from the coupling of hidden Berry curvature and hidden orbital polarization [59–61]. Very recently, the nontrivial transport response, originated from the coupling between the hidden Berry curvature and the Néel order, is reported, dubbed as layer Hall effect [62,63]. Overall, the non-reciprocal transport proposed here is a comprehensive demonstration of such effects, hopefully triggering future studies to unveil practical applications of hidden physical quantities.

[*]Corresponding author.
liuqh@sustech.edu.cn

[1] G. Dresselhaus, Spin-orbit coupling effects in zinc blende structures, Phys. Rev. **100**, 580 (1955).

[2] Y. A. Bychkov and E. I. Rashba, Properties of a 2D electron gas with lifted spectral degeneracy, JETP Lett. **39**, 78 (1984).

[3] Q. Liu, Y. Guo, and A. J. Freeman, Tunable Rashba effect in two-dimensional LaOBiS$_2$ films: Ultrathin candidates for spin field effect transistors, Nano Lett. 13, 5264 (2013).

[4] X. Zhang, Q. Liu, J.-W. Luo, A. J. Freeman, and A. Zunger, Hidden spin polarization in inversion-symmetric bulk crystals, Nat. Phys. 10, 387 (2014).

[5] Q. Liu, X. Zhang, H. Jin, K. Lam, J. Im, A. J. Freeman, and A. Zunger, Search and design of nonmagnetic centrosymmetric layered crystals with large local spin polarization, Phys. Rev. B 91, 235204 (2015).

[6] Y. Zhang, P. Liu, H. Sun, S. Zhao, H. Xu, and Q. Liu, Symmetry-assisted protection and compensation of hidden spin polarization in centrosymmetric systems, Chin. Phys. Lett. 37, 087105 (2020).

[7] R. Suzuki, M. Sakano, Y. J. Zhang, R. Akashi, D. Morikawa, A. Harasawa, K. Yaji, K. Kuroda, K. Miyamoto, T. Okuda, K. Ishizaka, R. Arita, and Y. Iwasa, Valley-dependent spin polarization in bulk MoS$_2$ with broken inversion symmetry, Nat. Nanotechnol. 9, 611 (2014).

[8] Q. Liu, X. Zhang, and A. Zunger, Intrinsic Circular Polarization in Centrosymmetric Stacks of Transition-Metal Dichalcogenide Compounds, Phys. Rev. Lett. 114, 087402 (2015).

[9] R. Gautier, J. M. Klingsporn, R. P. Van Duyne, and K. R. Poeppelmeier, Optical activity from racemates, Nat. Mater. 15, 591 (2016).

[10] J. H. Ryoo and C.-H. Park, Hidden orbital polarization in diamond, silicon, germanium, gallium arsenide and layered materials, NPG Asia Mater. 9, e382 (2017).

[11] S. Beaulieu, J. Schusser, S. Dong, M. Schuler, T. Pincelli, M. Dendzik, J. Maklar, A. Neef, H. Ebert, K. Hricovini, M. Wolf, J. Braun, L. Rettig, J. Minar, and R. Ernstorfer, Revealing Hidden Orbital Pseudospin Texture with Time-Reversal Dichroism in Photoelectron Angular Distributions, Phys. Rev. Lett. 125, 216404 (2020).

[12] S. Cho, J. H. Park, J. Hong, J. Jung, B. S. Kim, G. Han, W. Kyung, Y. Kim, S. K. Mo, J. D. Denlinger, J. H. Shim, J. H. Han, C. Kim, and S. R. Park, Experimental Observation of Hidden Berry Curvature in Inversion-Symmetric Bulk 2H-WSe$_2$, Phys. Rev. Lett. 121, 186401 (2018).

[13] Michael Schüler, Umberto De Giovannini, Hannes Hübener, Angel Rubio, Michael A. Sentef, and P. Werner, Local Berry curvature signatures in dichroic angle-resolved photoelectron spectroscopy from two-dimensional materials, Sci. Adv. 6, eaay2730 (2020).

[14] C. Wang, B. Lian, X. Guo, J. Mao, Z. Zhang, D. Zhang, B. L. Gu, Y. Xu, and W. Duan, Type-II Ising Superconductivity in Two-Dimensional Materials with Spin-Orbit Coupling, Phys. Rev. Lett. 123, 126402 (2019).

[15] Joseph Falson, Yong Xu, Menghan Liao, Yunyi Zang, Kejing Zhu, Chong Wang, Zetao Zhang, Hongchao Liu, Wenhui Duan, Ke He, Haiwen Liu, Jurgen H. Smet, Ding Zhang, and Q.-K. Xue, Type-II Ising pairing in few-layer stanene, Science 367, 1454 (2020).

[16] L. Yuan, Q. Liu, X. Zhang, J. W. Luo, S. S. Li, and A. Zunger, Uncovering and tailoring hidden Rashba spin-orbit splitting in centrosymmetric crystals, Nat. Commun. 10, 906 (2019).

[17] S. Guan, J.-X. Xiong, Z. Wang, and J.-W. Luo, Progress of hidden spin polarization in inversion-symmetric crystals, Sci. China Phys. Mech. Astron. 65, 237301 (2022).

[18] J. M. Riley, F. Mazzola, M. Dendzik, M. Michiardi, T. Takayama, L. Bawden, C. Granerød, M. Leandersson, T. Balasubramanian, M. Hoesch, T. K. Kim, H. Takagi, W. Meevasana, P. Hofmann, M. S. Bahramy, J. W. Wells, and P. D. C. King, Direct observation of spin-polarized bulk bands in an inversion-symmetric semiconductor, Nat. Phys. 10, 835 (2014).

[19] E. Razzoli, T. Jaouen, M. L. Mottas, B. Hildebrand, G. Monney, A. Pisoni, S. Muff, M. Fanciulli, N. C. Plumb, V. A. Rogalev, V. N. Strocov, J. Mesot, M. Shi, J. H. Dil, H. Beck, and P. Aebi, Selective Probing of Hidden Spin-Polarized States in Inversion-Symmetric Bulk MoS$_2$, Phys. Rev. Lett. 118, 086402 (2017).

[20] S. L. Wu, K. Sumida, K. Miyamoto, K. Taguchi, T. Yoshikawa, A. Kimura, Y. Ueda, M. Arita, M. Nagao, S. Watauchi, I. Tanaka, and T. Okuda, Direct evidence of hidden local spin polarization in a centrosymmetric superconductor LaO$_{0.55}$F$_{0.45}$BiS$_2$, Nat. Commun. 8, 1919 (2017).

[21] W. Yao, E. Wang, H. Huang, K. Deng, M. Yan, K. Zhang, K. Miyamoto, T. Okuda, L. Li, Y. Wang, H. Gao, C. Liu, W. Duan, and S. Zhou, Direct observation of spin-layer locking by local Rashba effect in monolayer semiconducting PtSe$_2$ film, Nat. Commun. 8, 14216 (2017).

[22] M. Gehlmann, I. Aguilera, G. Bihlmayer, E. Mlynczak, M. Eschbach, S. Doring, P. Gospodaric, S. Cramm, B. Kardynal, L. Plucinski, S. Blugel, and C. M. Schneider, Quasi 2D electronic states with high spin-polarization in centrosymmetric MoS$_2$ bulk crystals, Sci. Rep. 6, 26197 (2016).

[23] Kenneth Gotlieb, Chiu-Yun Lin, Maksym Serbyn, Wentao Zhang, Christopher L. Smallwood, Christopher Jozwiak, Hiroshi Eisaki, Zahid Hussain, Ashvin Vishwanath, and A. Lanzara, Revealing hidden spin-momentum locking in a high-temperature cuprate superconductor, Science 362, 1271 (2018).

[24] G. Gatti, D. Gosálbez-Martinez, S. Roth, M. Fanciulli, M. Zacchigna, M. Kalläne, K. Rossnagel, C. Jozwiak, A. Bostwick, E. Rotenberg, A. Magrez, H. Berger, I. Vobornik, J. Fujii, O. V. Yazyev, M. Grioni, and A. Crepaldi, Hidden bulk and surface effects in the spin polarization of the nodal-line semimetal ZrSiTe, Commun. Phys. 4, 54 (2021).

[25] H. J. Qian, X. Zhang, C. M. Liu, Q. Jiang, W. J. Liu, H. M. Zha, D. Y. Wang, X. P. Shen, M. Ye, Y. F. Guo, and S. Qiao, Layer-locked spin states revealed in the centrosymmetric nodal-line semimetal HfSiS, Phys. Rev. B 104, 035145 (2021).

[26] K. Zhang, S. Zhao, Z. Hao, S. Kumar, E. F. Schwier, Y. Zhang, H. Sun, Y. Wang, Y. Hao, X. Ma, C. Liu, L. Wang, X. Wang, K. Miyamoto, T. Okuda, C. Liu, J. Mei, K. Shimada, C. Chen, and Q. Liu, Observation of Spin-Momentum-Layer Locking in a Centrosymmetric Crystal, Phys. Rev. Lett. 127, 126402 (2021).

[27] L. L. Tao and E. Y. Tsymbal, Two-dimensional spin-valley locking spin valve, Phys. Rev. B 100, 161110(R) (2019).

[28] J. Zelezny, H. Gao, K. Vyborny, J. Zemen, J. Masek, A. Manchon, J. Wunderlich, J. Sinova, and T. Jungwirth, Relativistic Neel-Order Fields Induced by Electrical Current in Antiferromagnets, Phys. Rev. Lett. **113**, 157201 (2014).

[29] P. Wadley *et al.*, Electrical switching of an antiferromagnet, Science **351**, 587 (2016).

[30] C. C. Chiang, S. Y. Huang, D. Qu, P. H. Wu, and C. L. Chien, Absence of Evidence of Electrical Switching of the Antiferromagnetic Néel Vector, Phys. Rev. Lett. **123**, 227203 (2019).

[31] J. Godinho, H. Reichlova, D. Kriegner, V. Novak, K. Olejnik, Z. Kaspar, Z. Soban, P. Wadley, R. P. Campion, R. M. Otxoa, P. E. Roy, J. Zelezny, T. Jungwirth, and J. Wunderlich, Electrically induced and detected Neel vector reversal in a collinear antiferromagnet, Nat. Commun. **9**, 4686 (2018).

[32] Hiroki Isobe, Su-Yang Xu, and L. Fu, High-frequency rectification via chiral Bloch electrons, Sci. Adv. **6**, eaay2497 (2020).

[33] Y. Tokura and N. Nagaosa, Nonreciprocal responses from non-centrosymmetric quantum materials, Nat. Commun. **9**, 3740 (2018).

[34] See Supplemental Material at http://link.aps.org/supplemental/10.1103/PhysRevLett.129.276601 containing Boltzmann equation for NLC, NLC calculation with DFT, the characteristic of transverse NLC, critical temperature of NLC, the k_z-resolved NLC of bulk CuMnAs, the NLC of nonuple-layer $Mn_2Bi_2Te_5$, atomic orbitals projected band structures of CuMnAs film, which includes Refs. [35–41].

[35] G. Kresse and J. Furthmüller, Efficient iterative schemes for *ab initio* total-energy calculations using a plane-wave basis set, Phys. Rev. B **54**, 11169 (1996).

[36] G. Kresse and D. Joubert, From ultrasoft pseudopotentials to the projector augmented-wave method, Phys. Rev. B **59**, 1758 (1999).

[37] J. P. Perdew, K. Burke, and M. Ernzerhof, Generalized Gradient Approximation Made Simple, Phys. Rev. Lett. **77**, 3865 (1996).

[38] S. L. Dudarev, G. A. Botton, S. Y. Savrasov, C. J. Humphreys, and A. P. Sutton, Electron-energy-loss spectra and the structural stability of nickel oxide: An LSDA + U study, Phys. Rev. B **57**, 1505 (1998).

[39] A. A. Mostofi, J. R. Yates, Y.-S. Lee, I. Souza, D. Vanderbilt, and N. Marzari, wannier90: A tool for obtaining maximally-localised Wannier functions, Comput. Phys. Commun. **178**, 685 (2008).

[40] Q. Wu, S. Zhang, H.-F. Song, M. Troyer, and A. A. Soluyanov, WannierTools: An open-source software package for novel topological materials, Comput. Phys. Commun. **224**, 405 (2018).

[41] Y. Li, Y. Jiang, J. Zhang, Z. Liu, Z. Yang, and J. Wang, Intrinsic topological phases in $Mn_2Bi_2Te_5$ tuned by the layer magnetization, Phys. Rev. B **102**, 121107(R) (2020).

[42] H. Watanabe and Y. Yanase, Nonlinear electric transport in odd-parity magnetic multipole systems: Application to Mn-based compounds, Phys. Rev. Res. **2**, 043081 (2020).

[43] J. Železný, Z. Fang, K. Olejník, J. Patchett, F. Gerhard, C. Gould, L. W. Molenkamp, C. Gomez-Olivella, J. Zemen, T. Tichý, T. Jungwirth, and C. Ciccarelli, Unidirectional magnetoresistance and spin-orbit torque in NiMnSb, Phys. Rev. B **104**, 054429 (2021).

[44] S. S.-L. Zhang and G. Vignale, Theory of bilinear magneto-electric resistance from topological-insulator surface states, *Proc. SPIE* (SPIE, San Diego, 2018), Vol. 10732, p. 1073215.

[45] I. Sodemann and L. Fu, Quantum Nonlinear Hall Effect Induced by Berry Curvature Dipole in Time-Reversal Invariant Materials, Phys. Rev. Lett. **115**, 216806 (2015).

[46] T. Guillet, C. Zucchetti, Q. Barbedienne, A. Marty, G. Isella, L. Cagnon, C. Vergnaud, H. Jaffres, N. Reyren, J. M. George, A. Fert, and M. Jamet, Observation of Large Unidirectional Rashba Magnetoresistance in Ge(111), Phys. Rev. Lett. **124**, 027201 (2020).

[47] K. Olejník, V. Novák, J. Wunderlich, and T. Jungwirth, Electrical detection of magnetization reversal without auxiliary magnets, Phys. Rev. B **91**, 180402(R) (2015).

[48] C. O. Avci, K. Garello, A. Ghosh, M. Gabureac, S. F. Alvarado, and P. Gambardella, Unidirectional spin Hall magnetoresistance in ferromagnet/normal metal bilayers, Nat. Phys. **11**, 570 (2015).

[49] T. Ideue, K. Hamamoto, S. Koshikawa, M. Ezawa, S. Shimizu, Y. Kaneko, Y. Tokura, N. Nagaosa, and Y. Iwasa, Bulk rectification effect in a polar semiconductor, Nat. Phys. **13**, 578 (2017).

[50] D. F. Shao, S. H. Zhang, G. Gurung, W. Yang, and E. Y. Tsymbal, Nonlinear Anomalous Hall Effect for Néel Vector Detection, Phys. Rev. Lett. **124**, 067203 (2020).

[51] Peizhe Tang, Quan Zhou, Gang Xu, and S.-C. Zhang, Dirac fermions in an antiferromagnetic semimetal, Nat. Phys. **12**, 1100 (2016).

[52] L. Smejkal, J. Zelezny, J. Sinova, and T. Jungwirth, Electric Control of Dirac Quasiparticles by Spin-Orbit Torque in an Antiferromagnet, Phys. Rev. Lett. **118**, 106402 (2017).

[53] S.-G. Xu, Z.-J. Chen, X.-B. Chen, Y.-J. Zhao, H. Xu, and X. Zhang, Dirac fermions in the antiferromagnetic spintronics material CuMnAs, Phys. Rev. B **102**, 125123 (2020).

[54] C. Wang, Y. Gao, and D. Xiao, Intrinsic Nonlinear Hall Effect in Antiferromagnetic Tetragonal CuMnAs, Phys. Rev. Lett. **127**, 277201 (2021).

[55] H. Liu, J. Zhao, Y. X. Huang, W. Wu, X. L. Sheng, C. Xiao, and S. A. Yang, Intrinsic Second-Order Anomalous Hall Effect and Its Application in Compensated Antiferromagnets, Phys. Rev. Lett. **127**, 277202 (2021).

[56] R. Fei, W. Song, L. Pusey-Nazzaro, and L. Yang, *PT*-Symmetry-Enabled Spin Circular Photogalvanic Effect in Antiferromagnetic Insulators, Phys. Rev. Lett. **127**, 207402 (2021).

[57] H. Xu, H. Wang, J. Zhou, and J. Li, Pure spin photocurrent in non-centrosymmetric crystals: bulk spin photovoltaic effect, Nat. Commun. **12**, 1 (2021).

[58] Y. Gao, C. Wang, and D. Xiao, Topological Inverse Faraday Effect in Weyl Semimetals, arXiv:2009.13392.

[59] L. Du, Comment on "Disentangling Orbital and Valley Hall Effects in Bilayers of Transition Metal Dichalcogenides," Phys. Rev. Lett. **127**, 149701 (2021).

[60] T. P. Cysne, M. Costa, L. M. Canonico, M. B. Nardelli, R. B. Muniz, and T. G. Rappoport, Disentangling Orbital and Valley Hall Effects in Bilayers of Transition

Metal Dichalcogenides, Phys. Rev. Lett. **126,** 056601 (2021).

[61] T. P. Cysne, S. Bhowal, G. Vignale, and T. G. Rappoport, Orbital hall effect in bilayer transition metal dichalcogenides: From the intra-atomic approximation to the Bloch states orbital magnetic moment approach, Phys. Rev. B **105,** 195421 (2022).

[62] A. Gao *et al.*, Layer Hall effect in a 2D topological axion antiferromagnet, Nature (London) **595,** 521 (2021).

[63] R. Chen, H.-P. Sun, M. Gu, C.-B. Hua, Q. Liu, H.-Z. Lu, and X. C. Xie, Layer Hall effect induced by hidden Berry curvature in antiferromagnetic insulators, Natl. Sci. Rev. nwac140 (2022).